

# Can current models predict the local black hole merger rate?

Lumen Boco<sup>1</sup> \*, Michele Bosi<sup>2,3</sup> , Cecilia Sgalletta<sup>1</sup> , Amedeo Romagnolo<sup>1,4</sup> , Michela Mapelli<sup>1,4,5,6</sup> 

<sup>1</sup>Universität Heidelberg, Zentrum für Astronomie (ZAH), Institut für Theoretische Astrophysik, Albert Ueberle Str. 2, 69120, Heidelberg, Germany

<sup>2</sup>SISSA, Via Bonomea 365, I-34136 Trieste, Italy

<sup>3</sup>Department of Physics, University of Trento, Via Sommarive 14, 38123 Povo (TN), Italy

<sup>4</sup>Dipartimento di Fisica e Astronomia Galileo Galilei, Università di Padova, Vicolo dell'Osservatorio 3, I-35122 Padova, Italy

<sup>5</sup>Universität Heidelberg, Interdisziplinäres Zentrum für Wissenschaftliches Rechnen, D-69120 Heidelberg, Germany

<sup>6</sup>INFN, Sezione di Padova, Via Marzolo 8, I-35131 Padova, Italy

Received XXXX; accepted YYYY

## ABSTRACT

After four observational runs, the Ligo-Virgo-Kagra collaboration estimated a local binary black hole (BBH) merger rate density of  $R_{0,LVK} \approx 14 - 26 \text{ Gpc}^{-3} \text{ yr}^{-1}$  within the 90% credible interval. Some previous studies already pointed out that, when a realistic evolution of the metallicity-dependent cosmic star formation rate density (SFRD) is adopted, theoretical models predict a local BBH merger rate density that exceeds the observed value by at least a factor of  $\sim 10$  (Sgalletta et al. 2025). In this paper, we confirm and strengthen this claim by constructing an empirical model for the SFRD and metallicity evolution that includes a correction accounting for iron abundance. The adopted metallicity relation is flexible, enabling us to bracket the wide range of observational uncertainties. We show that, even under the most conservative assumptions regarding both the SFRD and the metallicity relation, the local BBH merger rate density is overestimated by a factor  $> 10$ . Attempts to reconcile the predicted and observed merger rates by modifying only the metallicity-dependent SFRD would require unrealistically high metallicities ( $Z > Z_{\odot}$ ) even in low-mass galaxies at high redshift. This finding indicates that revisions to the treatment of stellar and binary evolution are necessary to achieve consistency between theoretical predictions and observations. We suggest that even a modest steepening of the delay-time distribution could help alleviate this tension.

**Key words.** Gravitational Waves - Galaxies: abundances - Galaxies: evolution - Binaries: general - Stars: black holes

## 1. Introduction

It has now been more than ten years since the first gravitational wave (GW) detection by the LIGO–Virgo–KAGRA (LVK) collaboration. With the first four observing runs completed, we have started deriving with increasing precision the local binary black hole (BBH) merger rate density  $R_{0,LVK} \approx 14 - 26 \text{ Gpc}^{-3} \text{ yr}^{-1}$ , its evolution up to  $z \gtrsim 1$ , and the mass function of merging black holes (BHs, The LIGO Scientific Collaboration et al. 2025). From a theoretical perspective, the local BBH merger rate density has been estimated in numerous studies by combining a ‘stellar and binary-evolution term’ – representing the outcomes of binary population synthesis codes – with a metallicity-dependent star formation rate density SFRD( $z, Z$ ), derived either from cosmological simulations (Mapelli et al. 2017; O’Shaughnessy et al. 2017; Lamberts et al. 2018; Mapelli & Giacobbo 2018; Artale et al. 2019; Levina et al. 2026), or from empirical relations (Belczynski et al. 2016; Lamberts et al. 2016; Cao et al. 2018; Elbert et al. 2018; Li et al. 2018; Boco et al. 2019; Chruslinska & Nelemans 2019; Neijssel et al. 2019; Santoliquido et al. 2020; Boco et al. 2021; Santoliquido et al. 2022; Broekgaarden et al. 2022; Romagnolo et al. 2023, 2025; Sgalletta et al. 2025).

The role of SFRD( $z, Z$ ) is to provide a synthetic Universe within which binaries generated by population synthesis codes can evolve. It plays a fundamental role in determining the rate

and the properties of BBH mergers, as metallicity critically determines the fate of massive stellar binaries. Several studies (Chruslinska & Nelemans 2019; Boco et al. 2021; Chruslinska et al. 2021; Santoliquido et al. 2022; van Son et al. 2023; Sgalletta et al. 2025), accurately modeling the SFRD( $z, Z$ ) based on observations, highlighted that the metallicity distribution is not symmetric and features a pronounced tail towards low metallicities. This tail is primarily produced by low-mass galaxies and starbursts. The very existence of such a low-metallicity tail is relevant for BBH merger rates computations, as the BBH merger efficiency is strongly dependent on metallicity and reaches its maximum at low metallicities  $Z \lesssim Z_{\odot}/3$ . A careful characterization of the metallicity distribution is therefore essential for any robust computation of the BBH merger rate density. The shape of the metallicity distribution and the extension of the low-metallicity tail depend on the assumptions made in modeling galaxies, including the choice of the galaxies stellar mass function, the star-forming main sequence, the starburst fraction, and the metallicity relation (Boco et al. 2021; Chruslinska et al. 2021).

Sgalletta et al. (2025), using the binary population synthesis code `SEVN` and an up-to-date metallicity relation (Andrews & Martini 2013), show that the low-metallicity tail leads to an overestimation of the local BBH merger rates with respect to the observed rate  $R_{0,LVK}$  by a factor  $\gtrsim 10$ , independently of the adopted prescription for the main sequence of star-forming galaxies. The authors conclude that reconciling the predicted and observed lo-

\* lumen.boco@uni-heidelberg.de

cal merger rates requires modifications to the stellar and binary evolution term. Possible solutions include suppressing specific BBH formation channels, such as those involving a common-envelope phase (e.g., [Olejak et al. 2021](#); [Romagnolo et al. 2025](#)), or increasing the strength of natal kicks.

This prediction is even too optimistic: most calculations of the BBH merger rate density based on empirical metallicity scaling relations rely on oxygen abundances  $O/H$ , since oxygen is the primary tracer used to infer gas-phase metallicities in star-forming galaxies. However, line-driven stellar winds for  $Z \gtrsim 0.1 Z_{\odot}$  are driven by iron lines, while at lower metallicities their dependence on other driving elements is nearly completely unconstrained ([Romagnolo et al. 2026](#), and references therein). This implies that stellar and binary evolution are more sensitive to iron abundance than to oxygen. Oxygen-based metallicities are thus usually rescaled to a total metallicity  $Z$  by using solar relative abundances as a benchmark. However, several observations of star-forming galaxies ([Steidel et al. 2014, 2016](#); [Topping et al. 2020](#); [Sanders et al. 2021](#); [Cullen et al. 2021](#); [Strom et al. 2022](#)) and of local quiescent galaxies ([Thomas et al. 2005, 2010](#); [Johansson et al. 2012](#); [Álvarez et al. 2025](#)) show  $\alpha$ -enhancements up to  $O/Fe \sim 4 (O/Fe)_{\odot}$ . This enhancement arises because oxygen and iron have different enrichment timescales: oxygen is predominantly produced by core-collapse supernovae, while a substantial fraction of iron originates from Type Ia supernovae, which occur with a significant delay. Therefore, using solar abundance ratios to rescale oxygen and iron metallicities to a common global  $Z$  might lead to incorrect results. Specifically, this rescaling results in an overestimation of the iron abundance in all the  $\alpha$ -enhanced galaxies, potentially affecting predictions of BBH merger rates.

[Chruślińska et al. \(2024, 2025\)](#) provide an empirical calibration of the relative oxygen-to-iron abundance ratio  $O/Fe$  as a function of the galaxy specific star formation rate (sSFR), which tracks the age of the stellar population. This relation should be incorporated into models computing merger rates using oxygen-based metallicity relations. Implementing this correction would further reduce the inferred iron metallicity and, consequently, increase the predicted BBH merger rates, exacerbating the discrepancy highlighted by [Sgalletta et al. \(2025\)](#).

Here, we investigate the local BBH merger rate density  $\mathcal{R}_0$  by constructing a synthetic Universe using the empirical model proposed by [Boco et al. \(2021\)](#). We adopt the most conservative, sometimes even unrealistic, assumptions for the stellar mass function, the main sequence of star-forming galaxies, and the starburst distribution, with the aim of lowering  $\mathcal{R}_0$  as much as possible. We assign a gas-phase metallicity to our mock galaxies using the fundamental metallicity relation (FMR) derived by [Chruślińska et al. \(2021, hereafter Ch21\)](#), plus the correction of [Chruślińska et al. \(2025, hereafter Ch25\)](#), thus accounting for iron abundances for the first time in an empirical model. The FMR of [Ch21](#) provides a flexible parametrization that allows variations in key properties, such as its overall normalization and its dependence on galaxy stellar mass and star formation rate. We vary the FMR parameters bracketing the range spanned by the main metallicity relations present in literature ([Lara-López et al. 2010](#); [Mannucci et al. 2010](#); [Andrews & Martini 2013](#); [Salim et al. 2014](#); [Torrey et al. 2018](#); [Curti et al. 2020](#); [Sanders et al. 2021](#); [Curti et al. 2023](#); [Nakajima et al. 2023](#)), and we investigate whether, under reasonable metallicity variations, the local BBH merger rate density observed by LVK can be reproduced by models. We also investigate the impact of variations in the delay time distribution between the formation of the stellar binary and the merger of the remnant BHs.

The paper is structured as follows: in Section 2, we describe the methods used to compute the BBH merger rate density, with particular focus on the conservative choices made to minimize  $\mathcal{R}_0$ ; in Section 3, we present the results for reasonable variations of the FMR parameters; in Section 4, we reverse the approach and discuss about which assumptions and prescriptions should be used to reconcile the predicted and observed BBH merger rate; in Section 5, we summarize our main findings.

Throughout the paper we assume the Planck2018 cosmology, a flat Universe with  $H_0 \simeq 0.68$  and  $\Omega_m \simeq 0.31$ . We present results in terms of  $[X/H] \equiv \log(X/H) - \log(X/H)_{\odot}$ , where  $X$  is a generic element, in the present context either oxygen  $O$  or iron  $Fe$ . The reference solar abundances are from [Grevesse & Sauval \(1998\)](#), i.e.  $12 + \log(O/H)_{\odot} = 8.83$ ,  $12 + \log(Fe/H)_{\odot} = 7.5$ ,  $\log(O/Fe)_{\odot} = 1.33$ , and  $Z_{\odot} = 0.017$ , for consistency with [Ch25](#).

## 2. Methods

The BBH merger rate density at the cosmic time  $t$  can be computed as:

$$\mathcal{R}(t) = \int d \log Z \eta(Z) \int dt_d \frac{dp}{dt_d}(t_d|Z) \frac{d\dot{M}}{dV d \log Z}(t - t_d, Z) \quad (1)$$

where  $Z$  is the metallicity,  $t_d$  the delay time between the formation of the binary and the merger of the BH remnants,  $dp/dt_d$  is the delay time distribution, possibly dependent on metallicity,  $\eta(Z)$  is the BBH merger efficiency, defined as the number of BBHs formed per unit of star formation that have a delay time shorter than an Hubble time, and  $d\dot{M}/dV d \log Z$  is the metallicity-dependent star formation rate density SFRD( $z, Z$ ), computed at the time  $t - t_d$ . The merger efficiency and delay time distribution are usually computed from the outcomes of binary population synthesis codes. In this work we mainly adopt the results of the binary population synthesis code `SEVN`, fiducial model by [Iorio et al. \(2023\)](#), with common-envelope efficiency  $\alpha_{CE} = 1$ . However, in Section 3.3, we show the effect of varying the parameter  $\alpha_{CE}$ , and in Section 4.3 we compare our results with other studies using different binary population synthesis codes. We assume a binary fraction  $f_{\text{bin}} = 0.5$ , which is a conservative assumption as massive stars tend to feature higher binary fractions  $> 0.5$  ([Sana et al. 2012](#)).

The metallicity-dependent SFRD is computed by integrating the star formation rate (SFR) of all the galaxies in a given cosmological volume ([Boco et al. 2021](#)):

$$\begin{aligned} \frac{d\dot{M}}{dV d \log Z}(t, Z) &= \int_{\log M_{\star, \text{min}}} d \log M_{\star} \frac{dN(M_{\star}, t)}{dV d \log M_{\star}} \int d \log \psi \\ &\times \psi \frac{dp}{d \log \psi}(\log \psi | t, M_{\star}) \frac{dp}{d \log Z}(\log Z | M_{\star}, \psi) \end{aligned} \quad (2)$$

where  $dN/dV d \log M_{\star}$  is the star-forming galaxy stellar mass function (GSMF),  $\log M_{\star, \text{min}}$  is the minimum stellar mass accounted for in the integration,  $\psi$  is the SFR,  $dp/d \log \psi$  is the distribution of SFR at given mass and cosmic time and stellar mass, and  $dp/d \log Z$  is the metallicity distribution as a function of the galaxy stellar mass and SFR. We describe these elements in detail in the Sections below.

### 2.1. Galaxy stellar mass function (GSMF)

The GSMF  $dN/dV d \log M_{\star}$  represents the number density of galaxies per bin of stellar mass at different redshifts. It has been

determined by many observational studies (Ilbert et al. 2013; Muzzin et al. 2013; Tomczak et al. 2014; Davidzon et al. 2017; Weaver et al. 2023; Shuntov et al. 2025). We adopt the recent determination of the GSMF of star-forming galaxies by Weaver et al. (2023), derived from the COSMOS2020 catalog. For the sake of the BBH merger rate computation, the faint-end of the GSMF may be of some importance, as low-mass galaxies are poorer in metals and might host a significant number of BBH mergers. Therefore, the choice of the integration limit  $\log M_{\star, \min}$  in equation (2) is relevant. Since we want to provide a conservative estimate of  $\mathcal{R}_0$ , we choose  $M_{\star, \min} = 10^8 M_{\odot}$ , meaning that the contribution to the BBH merger rate density coming from all the galaxies with mass  $M_{\star} < 10^8 M_{\odot}$  is not kept into account.

## 2.2. SFR distribution

The galaxy SFR distribution  $dp/d \log \psi$  at given stellar mass and cosmic time can be computed from the main sequence of star-forming galaxies, a well-know correlation between stellar mass and SFR, which has been determined both observationally and theoretically in several works (Daddi et al. 2007; Rodighiero et al. 2011, 2015; Speagle et al. 2014; Whitaker et al. 2014; Schreiber et al. 2015; Mancuso et al. 2016; Dunlop et al. 2017; Bisigello et al. 2018; Pantoni et al. 2019; Lapi et al. 2020; Popesso et al. 2023; Bosi et al. 2025). Here, we adopt the relation by Popesso et al. (2023), one of the most recent observational determinations in a wide range of masses and redshift.

Despite the main sequence being the locus in the  $\log \psi - \log M_{\star}$  plane where most star forming galaxies are concentrated, the SFR distribution at fixed stellar mass and cosmic time is more complex. Many authors pointed out that this distribution tends to be bimodal, with a prominent peak representing main sequence galaxies, and a secondary peak at higher SFR representing starburst galaxies (Rodighiero et al. 2011; Béthermin et al. 2012; Sargent et al. 2012; Ilbert et al. 2015; Schreiber et al. 2015; Caputi et al. 2017; Bisigello et al. 2018; Rinaldi et al. 2022, 2025). This distribution is usually modeled with a double Gaussian in  $\log \psi$ , with the relative amplitude of the two Gaussians controlling the relative abundance of the two populations (Sargent et al. 2012; Boco et al. 2021). Several authors (Rodighiero et al. 2011; Béthermin et al. 2012; Sargent et al. 2012; Ilbert et al. 2015; Schreiber et al. 2015) estimated the fraction of starburst galaxies  $f_{\text{SB}}$  to be around  $\sim 3\%$ . However, most of these estimates were limited to most massive galaxies  $M_{\star} \gtrsim 10^{10} M_{\odot}$  at redshift  $z < 3$ . Recent studies (Caputi et al. 2017; Bisigello et al. 2018; Rinaldi et al. 2022, 2025) extended the mass and redshift range and pointed out that the starburst fraction tends to steeply increase at lower masses and higher redshift, reaching values of  $f_{\text{SB}} \gtrsim 90\%$  for  $M_{\star} \lesssim 10^7 M_{\odot}$  (Rinaldi et al. 2025). However, even galaxies with  $M_{\star} \gtrsim 10^8 M_{\odot}$  feature  $f_{\text{SB}} \sim 20 - 40\%$  at  $z \sim 3 - 6$ . Since starbursts have a SFR  $\sim 3 - 10$  times higher than main sequence galaxies and are typically metal poorer, these high values of  $f_{\text{SB}}$  may substantially increase BBH merger rates, as shown by Ch21. Here, as we aim to produce a conservative estimate of  $\mathcal{R}_0$ , we completely ignore the starburst population, setting  $f_{\text{SB}} = 0\%$ .

## 2.3. Metallicity distribution

The metal content of the cold star-forming gas in galaxies is of great importance to assess the masses and merger rates of BBHs, as the strength of line-driven winds for massive stars

critically depends on metallicity<sup>1</sup>. There are several observational relations between galaxy properties and gas-phase metallicity. These are usually given in terms of oxygen abundance  $12 + \log(\text{O}/\text{H})$ , whose emission lines are among the most luminous in the spectra of HII regions. Throughout this work we define  $Z_{\text{O}/\text{H}} \equiv 12 + \log(\text{O}/\text{H})$  and we assign a metallicity<sup>2</sup> to galaxies based on the fundamental metallicity relation, a relation between gas-phase metallicity, galaxy stellar mass and SFR (Lara-López et al. 2010; Mannucci et al. 2010, 2011; Andrews & Martini 2013; Zahid et al. 2014; Hunt et al. 2016; Cresci et al. 2019; Curti et al. 2020; Sanders et al. 2021; Boco et al. 2021; Chruślińska et al. 2021; Curti et al. 2023; Nakajima et al. 2023). The FMR has no explicit redshift dependence: the redshift evolution of metallicity at fixed stellar mass is implicitly accounted for through the metallicity-SFR anticorrelation. At higher redshift the average SFR of galaxies increases and thus the metallicity derived from the FMR decreases. This feature allows to use the FMR to compute metallicity even at high- $z$ , without the need of extrapolating the relation, as shown by Boco et al. (2021). The assumption of redshift independence of the FMR has been tested by multiple authors (Mannucci et al. 2010; Hunt et al. 2016; Curti et al. 2023; Nakajima et al. 2023), and its validity is somewhat dependent on the parametrization chosen. In particular, through a comparison with JADES and CEERS data, the FMR derived by Curti et al. (2020) has been recently proved to hold up to  $z \sim 4 - 6$ , while that by Andrews & Martini (2013) up to  $z \sim 8$  (Curti et al. 2023; Nakajima et al. 2023).

In this work, we use of the FMR parametrization introduced by Ch21. This is a flexible parametrization that makes use of the functional form of Curti et al. (2020), but with some free parameters that allow us to test the dependence of  $\mathcal{R}_0$  on different metallicity relations. The functional form of the FMR is the following:

$$Z_{\text{O}/\text{H}} = Z_{\text{O}/\text{H},0} - \frac{\gamma}{\beta} \log \left( 1 + \left( \frac{M_{\star}}{M_{0,\text{SFR}}} \right)^{-\beta} \right) \quad (3)$$

where  $Z_{\text{O}/\text{H},0}$  is a normalization, and the dependence on the SFR is enclosed in  $\log M_{0,\text{SFR}} \equiv m_0 + m_1 \log \psi$ . In the low-mass regime ( $M_{\star} \ll M_{0,\text{SFR}}$ ), it reduces to a linear relation in log:

$$Z_{\text{O}/\text{H}} \propto \gamma (\log M_{\star} - m_1 \log \psi) \propto \gamma \log M_{\star} - \nabla_{\text{FMR},0} \log \psi, \quad (4)$$

where  $\gamma$  is the slope of the correlation between metallicity and stellar mass, while  $\nabla_{\text{FMR},0} \equiv \gamma m_1$  is the slope of the anticorrelation between metallicity and SFR. This is the same functional form derived by Mannucci et al. (2010, 2011); Andrews & Martini (2013); Hunt et al. (2016). Ch21 demonstrated that, in the low-mass regime,  $\gamma$  and  $\nabla_{\text{FMR},0}$  are connected to the slope of the MZR  $a_{\text{MZR}}$  and the slope of the main sequence  $a_{\text{MS}}$ , computed at  $z = 0$ , by the following relation:  $\gamma = \nabla_{\text{FMR},0} a_{\text{MS}} + a_{\text{MZR}}$ . Since we have selected the main sequence determination of Popesso et al. (2023), which has a faint-end slope  $a_{\text{MS}} \sim 1$  at  $z = 0$ , this relation reduces to  $\gamma = \nabla_{\text{FMR},0} + a_{\text{MZR}}$ . Also the parameter  $m_0$  can be derived from the shape of the MZR and main sequence, though with a more complicated expression (see Ch21 for more details). Thus, the shape of the FMR can be entirely derived from

<sup>1</sup> Cool supergiant winds, instead, are not driven by lines, but likely by factors such as near-surface convective boil-off (Fuller & Tsuna 2024) and turbulence (Kee et al. 2021), remaining therefore of similar strength across different metallicity environments (Antoniadis et al. 2025).

<sup>2</sup> When talking about the FMR we use the term metallicity, or gas-phase metallicity, but we are referring to the oxygen abundance  $Z_{\text{O}/\text{H}}$ .

Parameter	Description	Values
$a_{\text{MZR}}$	Slope of the $z = 0$ MZR	0.15–0.3–0.6
$\nabla_{\text{FMR},0}$	Strength of $Z$ –SFR anti-correlation	0.2–0.3
$Z_{\text{O/H},0}$	FMR normalization	8.8–9.0–9.2
$\gamma$	Strength of $Z - M_*$ correlation	$a_{\text{MZR}} + a_{\text{MS}}$
$m_0$	Position of the FMR knee	Eq. 6 in Ch21
$m_1$	Dependence of knee on SFR	$\nabla_{\text{FMR},0}/\gamma$
$\beta$	Width of the FMR knee	2.1 (Curti et al. 2020)

**Table 1.** Description of the parameters and values adopted in this work. We vary  $a_{\text{MZR}}$ ,  $\nabla_{\text{FMR},0}$ , and  $Z_{\text{O/H},0}$  among the values reported in the Table.  $\gamma$ ,  $m_0$ ,  $m_1$ , and  $\beta$  are computed as written in the Table.

the local MZR and main sequence once a value for the parameter  $\nabla_{\text{FMR},0}$  is specified. We will vary the parameters  $a_{\text{MZR}}$  and  $\nabla_{\text{FMR},0}$  in reasonable ranges, and use them to derive the FMR parameters  $\gamma$ ,  $m_1 \equiv \nabla_{\text{FMR},0}/\gamma$  and  $m_0$ . We also vary the overall normalization  $Z_{\text{O/H},0}$ . The choices for these parameters are summarized in Table 1. In Appendix A we show that these choices brackets most of the values found in the literature. Since the FMR is redshift independent, we use it to compute metallicities at high redshift.

Finally, the scatter used around the FMR,  $\sigma_{\text{FMR}}$ , is important for the merger rate calculation, as it influences the extension of the low metallicity tail. A larger value of  $\sigma_{\text{FMR}}$  implies more star formation at low-metallicity, and thus a larger  $\mathcal{R}_0$ . Various FMR estimations report values of  $\sigma_{\text{FMR}}$  in the range 0.05–0.15. Despite recent JADES and CEERS data (Nakajima et al. 2023; Curti et al. 2023) have confirmed the validity of the FMR up to  $z \sim 4 - 8$ , the scatter around this relation seems to increase at high redshift. In this work we use  $\sigma_{\text{FMR}} = 0.05$  at all redshift to minimize the value of  $\mathcal{R}_0$ . Note that many models computing merger rates describe the metallicity in a ‘cosmic-averaged’ way, by selecting an average metallicity at each redshift  $\langle Z(z) \rangle$  and introducing a scatter around it, either with a log-normal distribution or with a skewed log-normal. We caution that  $\sigma_{\text{FMR}}$  reported here is not the same  $\sigma$  reported in those models.  $\sigma$  of the ‘cosmic-averaged’ models accounts for the overall metallicity dispersion at a fixed redshift, while  $\sigma_{\text{FMR}}$  is meant to render the possible dispersion of metallicity around the FMR, i.e. the dispersion for galaxies with the same stellar mass and SFR. The overall dispersion at a given redshift,  $\sigma$ , will be way larger than  $\sigma_{\text{FMR}}$ , and it is driven by the metallicities of individual galaxies with different  $M_*$  and SFR (see discussion in 4.3).

### 2.3.1. Iron and oxygen abundances

Most of the studies computing merger rates use the total metal mass fraction  $Z$  in equation (1). However, as mentioned in Section 1, this might be misleading. Iron-group elements’ abundances regulate stellar opacity and the strength of line-driven winds. Therefore, results of binary population synthesis codes, such as the merger efficiency  $\eta(Z)$  and delay time distribution  $dP/dt_d(t_d|Z)$ , are actually most impacted by the iron abundance rather than by the total metallicity. On the other hand, as highlighted above, observations of star-forming galaxies typically constrain oxygen abundance. Iron and oxygen abundances are generally converted to total metallicity using the solar relative abundances as a reference scale (e.g.,  $Z = Z_\odot 10^{[\text{O/H}]}$ ).

However, oxygen and iron have different enrichment timescales, with oxygen being produced mostly by massive stars, and thus tracing the SFR, while iron receiving a substantial contribution by type Ia supernovae (SNIa), which might have a longer delay time. This leads some galaxies, especially the

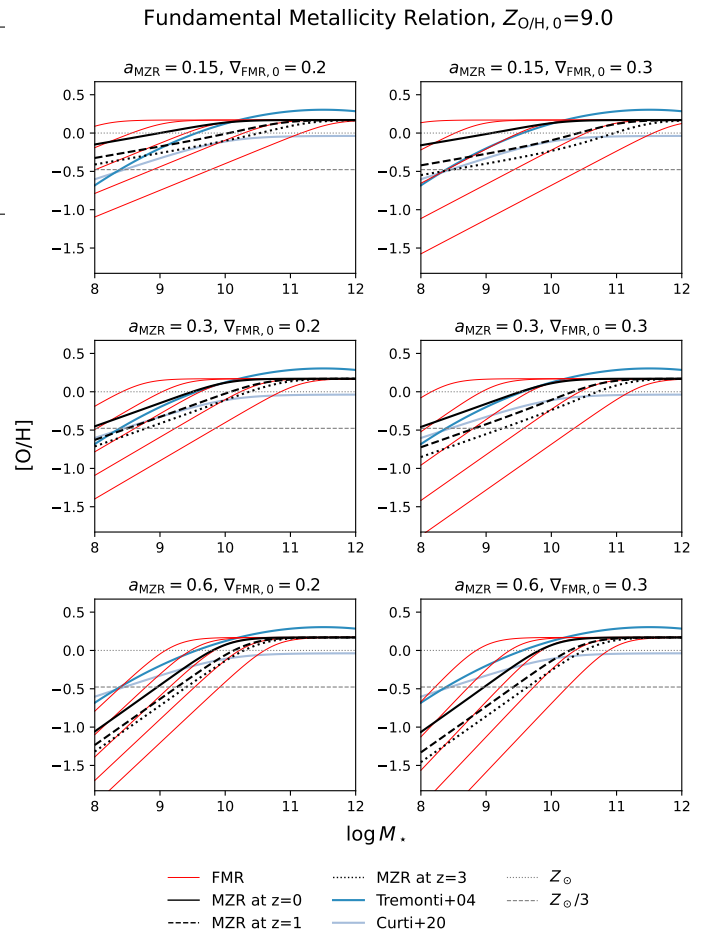


**Fig. 1.** The Fundamental Metallicity Relation (FMR) and the derived Mass Metallicity Relation (MZR) for  $Z_{\text{O/H},0} = 9.0$ , in terms of  $[\text{O/H}]$ . Different panels are for different values of  $a_{\text{MZR}}$  and  $\nabla_{\text{FMR},0}$ . Red thin lines show the FMR at different SFR,  $\log \psi = -3, -1.5, 0, 1.5, 3$  from the top to the bottom line. Black lines (solid, dashed and dotted) show the derived MZR at  $z = 0, 1, 3$ , respectively. The blue lines are  $z = 0$  MZR from the literature: Tremonti et al. (2004) dark blue, Curti et al. (2020) steel blue. Gray dashed and dotted horizontal lines represent  $Z_\odot/3$  and  $Z_\odot$ .

youngest, to be  $\alpha$ -enhanced with respect to solar abundance. High values of  $\alpha$ -enhancement have been measured in high redshift star-forming galaxies (Steidel et al. 2014, 2016; Topping et al. 2020; Sanders et al. 2021; Cullen et al. 2021; Strom et al. 2022), as well as in the stellar metallicity of local ellipticals (Thomas et al. 2005, 2010; Johansson et al. 2012; Álvarez et al. 2025), which are formed in short and intense bursts of star formation and quenched before SNIa had the time to enrich the interstellar medium with iron (Chiappini et al. 1997; Gallazzi et al. 2006; Thomas et al. 2005, 2010; Johansson et al. 2012; Courteau et al. 2014; Pezzulli & Fraternali 2016; Bellstedt et al. 2024; Álvarez et al. 2025).

Chruślińska et al. (2024) and Ch25 derive a handy empirical relationship between the O/Fe ratio and the galaxy specific SFR ( $s\text{SFR} \equiv \psi/M_*$ ), as the latter quantity is a proxy for the galaxy age. Here, we use the O/Fe–sSFR relation by Ch25, in the ‘Mixed’ Fe enrichment case. We use this relation to evaluate  $[\text{O/Fe}]$  as a function of the stellar mass and SFR of the galaxy, and we compute the iron abundance as  $[\text{Fe/H}] = [\text{O/H}] - [\text{O/Fe}]$ , where  $[\text{O/H}] = Z_{\text{O/H}} - Z_{\text{O/H},\odot}$  is derived from the FMR. The total metallicity  $Z$ , entering in equations (1) and (2), is then com-

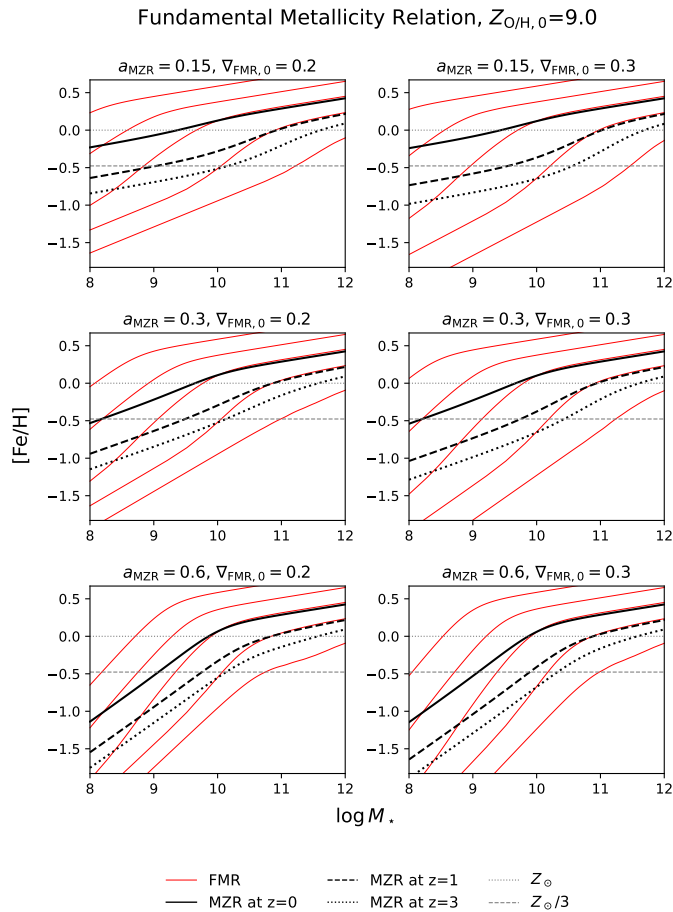


Fig. 2. Same as Figure 1, but for [Fe/H].

puted rescaling the iron abundance as:  $Z = Z_{\odot} 10^{[\text{Fe}/\text{H}]}$ . The metallicity distribution  $dp/d\log Z$  will be a Gaussian distribution, with a scatter  $\sigma_{\text{FMR}} \sim 0.05$ , as discussed in Section 2.3. Rescaling to iron abundance through the relation by Ch25 may introduce another source of scatter. We ignore this possible additional scatter as it would contribute to the low metallicity tail of the  $\text{SFRD}(z, Z)$ , thus increasing  $\mathcal{R}_0$ .

### 3. Results

#### 3.1. The fundamental metallicity relation

Figure 1 shows the FMR in terms of [O/H], derived for  $a_{\text{MZR}} = 0.15, 0.3, 0.6$  and  $\nabla_{\text{FMR},0} = 0.2, 0.3$ . The normalization  $Z_{\text{O}/\text{H},0}$  is fixed at 9.0, representing the middle of the three values considered 8.8, 9.0, 9.2. The other two values would correspond to a shift of  $\pm 0.2$  dex of the whole relation. The slope of the correlation with the stellar mass,  $\gamma$ , and the separation between the curves at different SFR,  $m_1$ , are regulated by the two input parameters  $a_{\text{MZR}}$  and  $\nabla_{\text{FMR},0}$ . The Figure also shows the MZR associated to that FMR and its average redshift evolution:

$$Z_{\text{MZR}}(M_{\star}, z) = \int d\log \psi \frac{dp}{d\log \psi}(\log \psi|z, M_{\star}) Z_{\text{FMR}}(M_{\star}, \psi). \quad (5)$$

For comparison, we also show the  $z = 0$  MZR by Tremonti et al. (2004); Andrews & Martini (2013) and Curti et al. (2020). The redshift evolution of the MZR is regulated by the parameter  $m_1$ ,

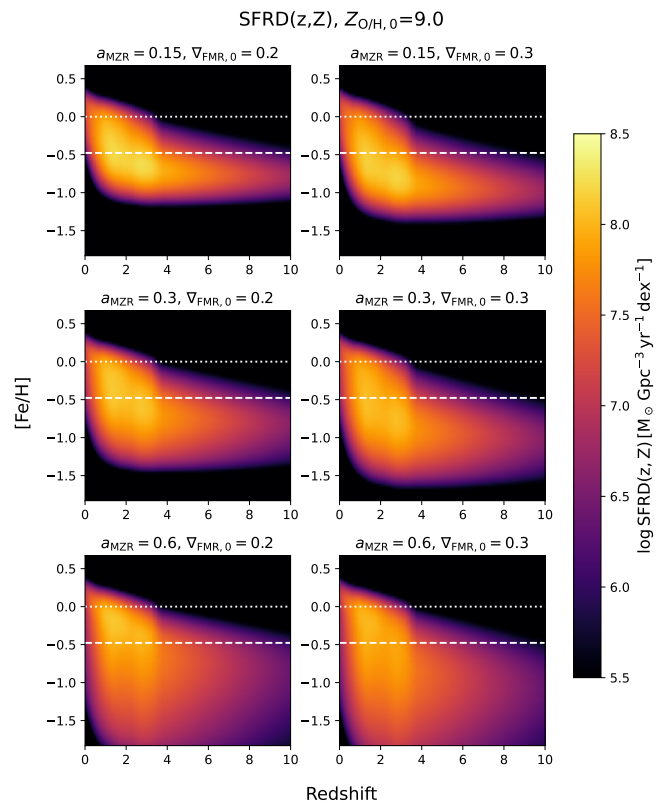


Fig. 3. Cosmic SFRD per metallicity bin ( $d\dot{M}/dV d\log Z$ ), for  $Z_{\text{O}/\text{H},0} = 9.0$ , as a function of  $z$  and [Fe/H]. Different panels are for different values of  $a_{\text{MZR}}$  and  $\nabla_{\text{FMR},0}$ . The white dashed and dotted horizontal lines represent  $Z_{\odot}/3$  and  $Z_{\odot}$ . We can see that the low-metallicity tail reduces for lower values of  $a_{\text{MZR}}$  and  $\nabla_{\text{FMR},0}$ .

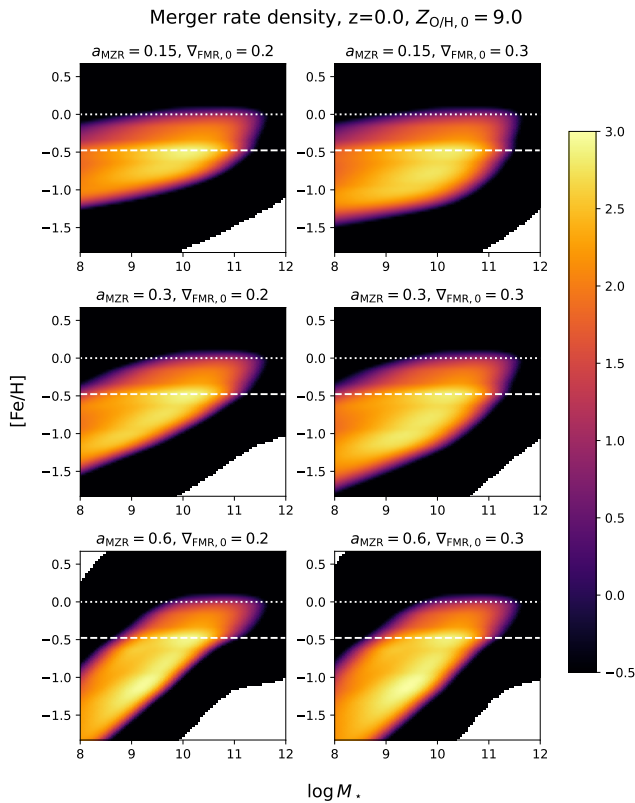
which sets the separation between the curves at different SFR, and thus it is governed by the input  $\nabla_{\text{FMR},0}$ .

Figure 2 displays the same relations but in terms of [Fe/H], i.e. with the Ch25 O/Fe correction.

The  $\text{SFRD}(z, Z)$  associated with the different metallicity relations is shown in Figure 3, in terms of [Fe/H]. It features a quite broad peak at  $1 < z < 3$ , the cosmic noon. The average [Fe/H] evolves with redshift: at  $z = 0$  it ranges from  $\sim Z_{\odot}/2$  to slightly supersolar, depending on the metallicity parameters chosen, at  $z \sim 4$  it ranges from  $\sim Z_{\odot}/10$  to  $\sim Z_{\odot}/5$ . Models with different  $Z_{\text{O}/\text{H},0}$  are simply shifted upwards or downwards by 0.2 dex. This redshift evolution is partly due to the decrease of average stellar mass and increase of SFR of galaxies at higher redshift, and partly to the [Fe/O] correction that is larger for high- $z$  galaxies, featuring higher average sSFR. At  $z > 4$ , the redshift evolution is shallower because the increase of SFR with redshift saturates. The distribution is not symmetric, but features a low-metallicity tail, which becomes more extended as  $a_{\text{MZR}}$  and  $\nabla_{\text{FMR},0}$  increase. A larger  $a_{\text{MZR}}$  means that low-mass galaxies are more metal poor, resulting in a more extended low-metallicity tail. A larger  $\nabla_{\text{FMR},0}$  means a stronger anti-correlation with SFR. This implies a more prominent low-metallicity tail, originated by more star forming galaxies, and a slightly faster redshift evolution of metallicity.

#### 3.2. The BBH merger rate density

The local BBH merger rate density  $\mathcal{R}_0$  receives contributions not only from the local SFRD, but also from BBHs formed at higher



**Fig. 4.** BBH merger rate density per metallicity and stellar mass bin ( $dN/dV d \log M_{\star} d \log Z$  at  $z = 0$ , as a function of  $\log M_{\star}$  and  $[Fe/H]$ ). Different panels are for different values of  $a_{MZR}$  and  $\nabla_{FMR,0}$ . The white dashed and dotted horizontal lines represent  $Z_{\odot}/3$  and  $Z_{\odot}$ . The contribution to the BBH merger rate density comes almost exclusively from  $Z < Z_{\odot}$  and is larger for  $Z < Z_{\odot}/3$ , due to the behavior of the merger efficiency  $\eta(Z)$ . The  $z = 0$  BBH merger rate density is reduced as  $a_{MZR}$  and  $\nabla_{FMR,0}$  decrease.

redshift that merge at  $z = 0$ . In particular, the high SFRD at cosmic noon contributes significantly to the number of mergers occurring at  $z = 0$ . The convolution of the SFRD with the delay-time distribution multiplied by the efficiency  $\eta(Z)$  gives the merger rate density of BBH.

Figure 4 shows the merger rate density at  $z = 0$  per unit of galaxy stellar mass and metallicity  $dN/dV d \log M_{\star} d \log Z$  and tells us the stellar mass and metallicity of the galaxies where BBHs merging at  $z = 0$  are formed. The integral of this quantity over  $M_{\star}$  and  $Z$  gives the local BBH merger rate density  $\mathcal{R}_0$ . The dependence of the merger rate density on metallicity reflects the behavior of the efficiency factor  $\eta(Z)$ . This factor is derived from binary population synthesis codes and usually it features an almost constant value  $\sim 10^{-4.5}$  at  $Z < Z_{\odot}/3$ , while it rapidly decreases for  $Z \gtrsim Z_{\odot}/3$ . Thus, the local BBH merger rate density is mostly determined by the amount of star formation occurring at metallicities lower than this threshold. Minimizing the amount of star formation occurring at  $Z < Z_{\odot}/3$  is the key to reduce the BBH merger rate for our default binary evolution models. Variations with lower  $a_{MZR}$ , lower  $\nabla_{FMR,0}$  and larger  $Z_{O/H,0}$  feature a less extended tail at low metallicity and imply lower  $\mathcal{R}_0$  values.

Figure 5 shows the BBH merger rate density as a function of redshift for all the model variations. From this Figure it is apparent that, independently of the chosen metallicity parameters, the local BBH merger rate density estimated by the models is well above the 90% credible interval inferred by the LVK col-

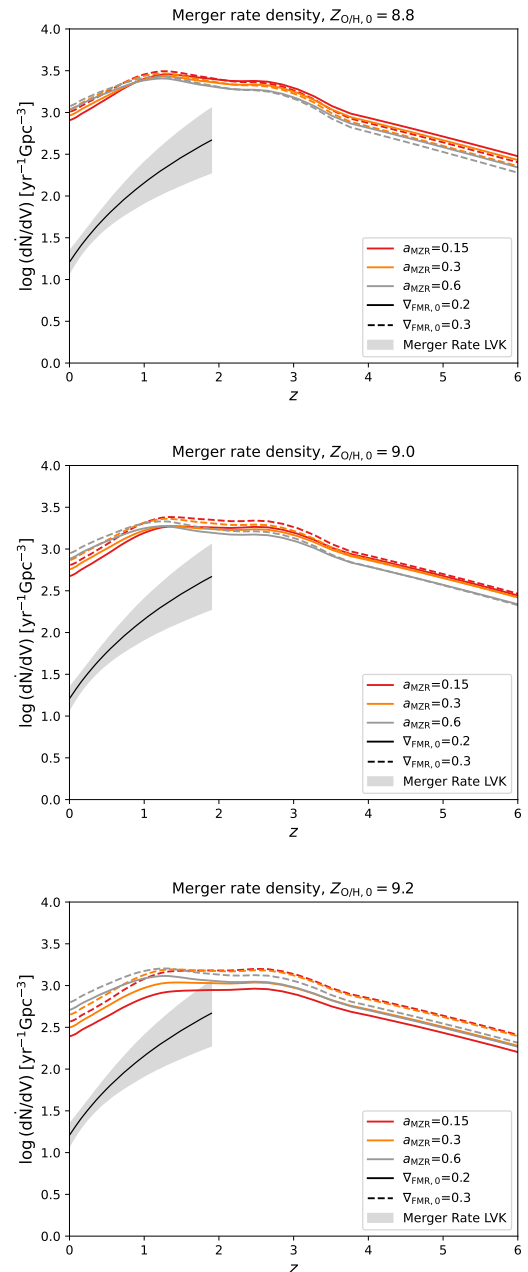
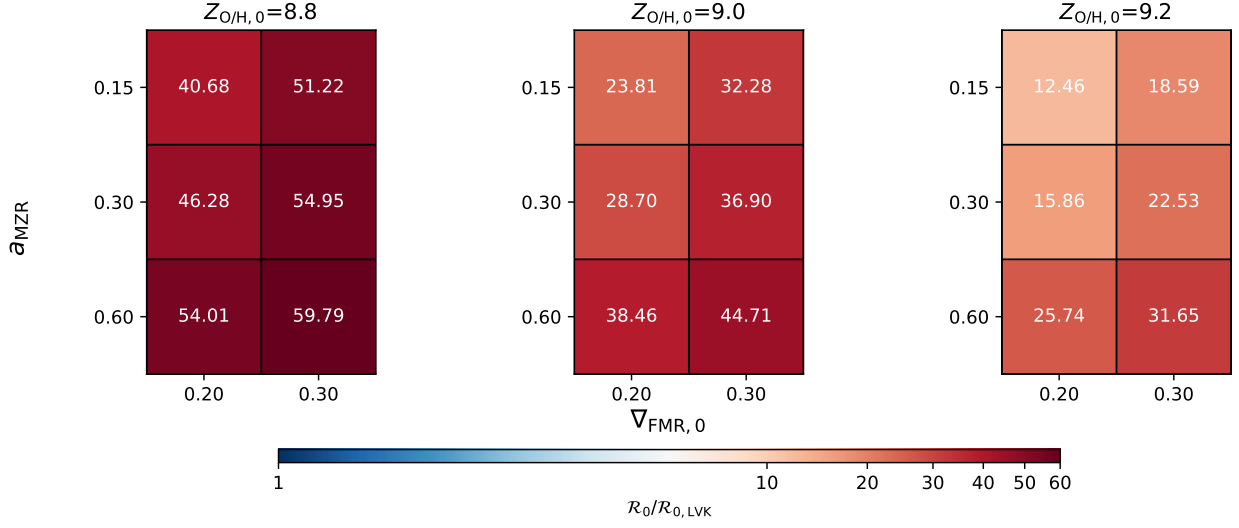


**Fig. 5.** BBH merger rate density as a function of redshift for  $Z_{O/H,0} = 8.8, 9.0, 9.2$  (top, middle, bottom panels),  $a_{MZR} = 0.15, 0.3, 0.6$  (red, orange, grey lines), and  $\nabla_{FMR,0} = 0.2, 0.3$  (solid, dashed lines). The black shaded area shows the merger rate density measured by LVK.

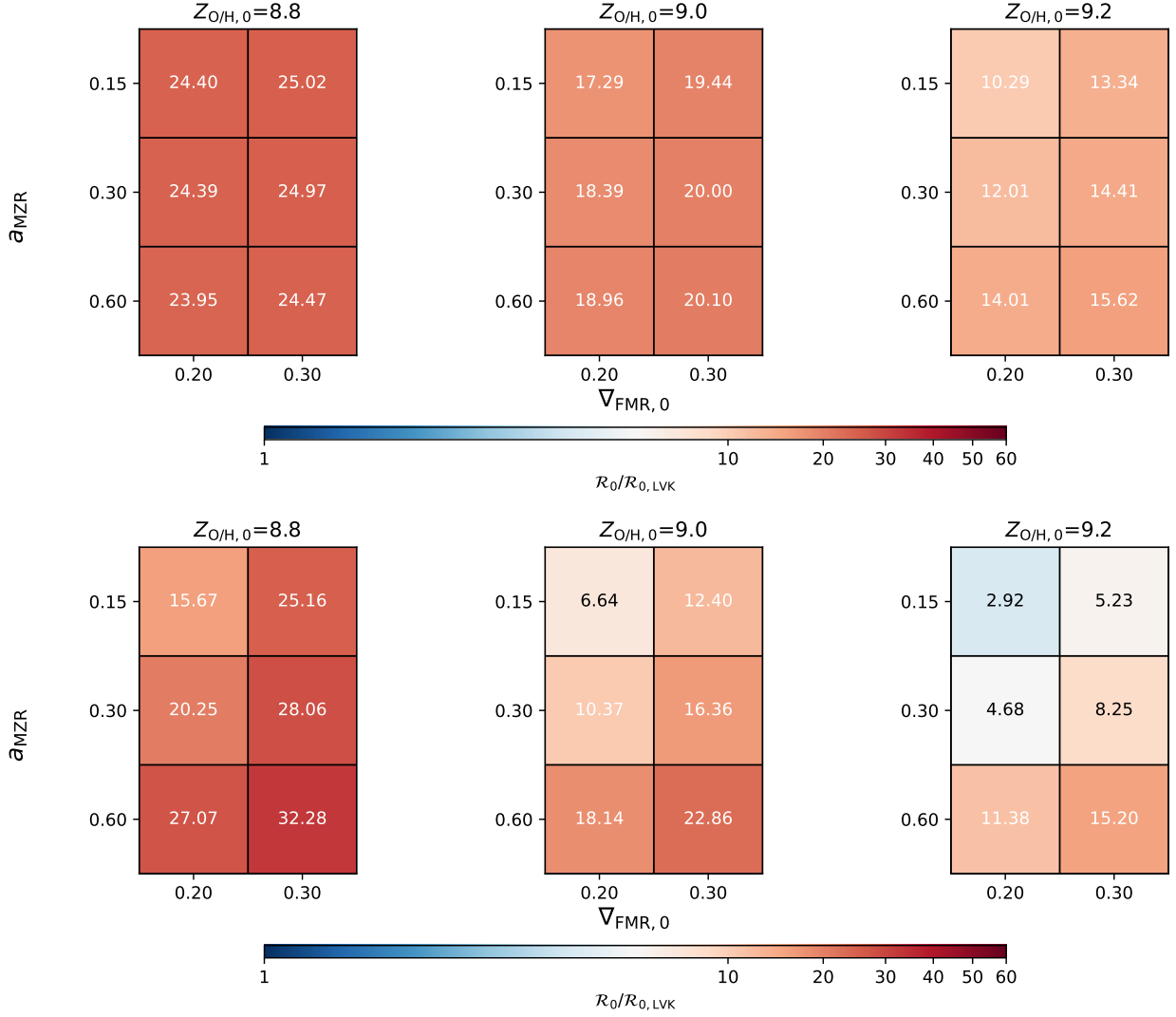
laboration. We note that also the slope is quite flatter than that predicted by observations.

Figure 6 displays a matrix indicating the ratio between the theoretical estimation and the observed local rate, as a function of the parameters of the metallicity relation. We can see that even in the most optimistic case, for  $Z_{O/H,0} = 9.2$ ,  $a_{MZR} = 0.15$ ,  $\nabla_{FMR,0} = 0.2$ , this ratio is  $\gtrsim 10$ .

Note that these results are obtained by considering only the isolated binary merger scenario, i.e. we consider that star formation only occurs in the field and completely neglect the effect of dynamics in young, globular or nuclear star clusters. Since dynamical interactions enhance the BBH merger efficiency, including these effects would only worsen the tension between mod-



**Fig. 6.** Matrix showing the ratio  $\mathcal{R}_0/\mathcal{R}_{0,\text{LVK}}$  for  $Z_{\text{O/H},0} = 8.8, 9.0, 9.2$  (left, middle, right tables),  $a_{\text{MZR}} = 0.15, 0.3, 0.6$  (y axis), and  $\nabla_{\text{FMR},0} = 0.2, 0.3$  (x-axis). The color scale is set so that it is blue for  $\mathcal{R}_0/\mathcal{R}_{0,\text{LVK}} = 1$ , and remains blue-shaded for  $\mathcal{R}_0/\mathcal{R}_{0,\text{LVK}} \leq 2$ , which corresponds to a distance of around  $\sim 6\sigma$  from the interval provided by LVK. For  $\mathcal{R}_0/\mathcal{R}_{0,\text{LVK}} > 2$  the color becomes redder and redder. No reasonable value of the FMR parameters can match  $\mathcal{R}_{0,\text{LVK}}$ .



**Fig. 7.** Same as Figure 6, but for  $\alpha_{\text{CE}} = 0.1$  (top panel) and  $\alpha_{\text{CE}} = 10$  (bottom panel).  $\mathcal{R}_{0,\text{LVK}}$  can be marginally matched for  $\alpha = 10$ ,  $Z_{\text{O/H},0} = 9.2$  and the lowest  $a_{\text{MZR}}$  and  $\nabla_{\text{FMR},0}$ .

els and data. The isolated binary merger scenario should either match or underestimate  $\mathcal{R}_{0,\text{LVK}}$ , not overestimate it.

We recall that all the assumptions and parameters to compute the SFRD( $z, Z$ ) have been chosen with the aim of trying to minimize the merger rates. This result demonstrates that no reasonable variation of the metallicity relation can reconcile the predicted value of the local BBH merger rate density with that inferred from LVK data. Our conclusion is that only some modifications in the treatment of single stellar and binary evolution can improve the agreement between predicted and observed BBH merger rate density. As for single stellar evolution, a possibility is to change the wind treatment used in population synthesis codes, possibly decreasing the threshold metallicity at which  $\eta(Z)$  drops (van Son et al. 2025). Several recent theoretical and observational works have shown that massive stars can develop optically thick winds (Vink et al. 2011; Bestenlehner et al. 2014; Bestenlehner 2020; Brands et al. 2022, 2025; Sabhahit et al. 2022, 2023; Romagnolo et al. 2024; Gormaz-Matamala et al. 2025; Simonato et al. 2025; Shepherd et al. 2025; Boco et al. 2025; Romagnolo et al. 2026; Tornamenti et al. 2026), even at relatively low metallicities  $\sim Z_{\odot}/5$  (Boco et al. 2025), where mass-loss can reach values as high as  $10^{-3} M_{\odot} \text{ yr}^{-1}$ . As for binary evolution, a first possibility is to increase the strength of supernova natal kicks (see discussion in Section 4.3 and Figure 7 in Sgalletta et al. 2025). Other options include to drastically update the description of mass transfer, of the common-envelope evolutionary phase (Olejak et al. 2021), and the treatment of tides.

### 3.3. The role of $\alpha_{\text{CE}}$

The results shown in the previous Section are obtained assuming a common-envelope efficiency parameter  $\alpha_{\text{CE}} = 1$ . Different values of  $\alpha$  may change the BBH merger rate density as they alter the efficiency of common-envelope ejection. A smaller value of  $\alpha$  leads to more stellar systems merging during the common-envelope phase, thus reducing the number of available BBHs. A larger value of  $\alpha$ , instead, leads to less shrinking of the binaries and produces less BBH systems with short initial orbital period.

Figure 7 shows the results of our analysis for  $\alpha_{\text{CE}} = 0.1$  and  $\alpha_{\text{CE}} = 10$ , taken as two extreme values. The predicted merger rate density is more compatible with the values inferred by LVK data for both cases. In particular, the  $\alpha = 10$  case shows a stronger dependence on metallicity and can drastically reduce the merger rate for the highest metallicity cases. Though, even with such an extreme  $\alpha_{\text{CE}}$  value, the most optimistic case yields  $\mathcal{R}_0/\mathcal{R}_{0,\text{LVK}} \sim 3$ . We conclude that variations of the common envelope efficiency are not enough to reconcile the predicted and observed rates (Sgalletta et al. 2025).

## 4. Discussion

### 4.1. Reversing the problem: what should the metallicity be to reconcile the local BBH merger rates?

Sgalletta et al. (2025) have recently showed that for any reasonable variation of the star-forming galaxy main sequence the local BBH merger rates cannot be reconciled with observations. Here, we go even further and show that for any reasonable variation of the metallicity relation, local BBH merger rates are overestimated, even making the most conservative choices for the GSFM and starburst fraction. In this Section, we address the following question: what should the values of the parameters of the metallicity relations (FMR and MZR) be in order to match  $\mathcal{R}_{0,\text{LVK}}$ ? To answer this question we extend the parameter space consid-

ered, exploring regions with  $a_{\text{MZR}} = 0.05$  and  $\nabla_{\text{FMR},0} = 0, 0.1$ . These values are quite unrealistic, as they yield metallicities way higher than any observationally-derived metallicity relation. Figure 8 shows a new matrix with the results of this approach. First of all, we can see that, even with these extreme variations, only the case with  $Z_{\text{O/H},0} = 9.2$ ,  $\nabla_{\text{FMR},0} = 0$ , and  $a_{\text{MZR}} = 0.05, 0.15$  leads to a reasonable agreement with the observed BBH merger rate.

The metallicity relation associated to the  $\nabla_{\text{FMR},0} = 0$ ,  $a_{\text{MZR}} = 0.15$  case is shown in Figure 9, in terms of  $[\text{O}/\text{H}]$ . Matching the local BBH merger rate density would require extremely high metallicities, both in terms of normalization, and in terms of steepness of the relation, implying that galaxies with mass  $M_{\star} = 10^8 M_{\odot}$  should have an average oxygen abundance around the solar value. This value is higher than what found in observations, which indicate metallicities in the range  $\sim 0.2 - 0.3 Z_{\odot}$  for  $M_{\star} = 10^8 M_{\odot}$  galaxies at  $z = 0$ . Even more importantly, the absence of a correlation with SFR ( $\nabla_{\text{FMR},0} = 0$ ) implies that metallicity should not evolve with redshift, meaning that these large metallicity values are the same at higher redshift.

### 4.2. The effect of merger efficiency and delay-time distribution

Here, we explore how the merger efficiency and the delay time distribution affect  $\mathcal{R}_0$ . Specifically, we investigate which efficiencies and delay times can reconcile the predictions of the local BBH merger rate with observations.

To this end, we vary the merger efficiency and the delay time distribution separately, while keeping the other quantity fixed. Specifically, we lower the merger efficiency while keeping the delay time distribution unvaried, and we steepen the delay time distribution while keeping  $\eta(Z)$  unvaried.

As the merger efficiency remains nearly constant for  $Z < Z_{\odot}/3$ , and declines sharply at higher metallicity, it acts as a multiplicative factor in the computation of the merger rates. Consequently, rescaling the low-metallicity merger efficiency by a given factor results in an equivalent rescaling of the predicted merger rate density. From Figure 6, we can see that matching  $\mathcal{R}_{0,\text{LVK}}$  would require a reduction of  $\eta(Z)$  by a factor  $\gtrsim 10$ .

An alternative approach is to further decrease the metallicity threshold above which the merger efficiency drops significantly, thereby excluding a larger fraction of the SFRD from contributing to BBH mergers. The redshift evolution of the BBH merger rates and the observed properties of BBHs can discriminate between these two alternatives (see Bosi et al. 2026, in prep.).

As for the delay time distribution, we assume a power-law scaling  $\propto t_d^{-\alpha}$  and we steepen the exponent  $\alpha$  until an agreement with  $\mathcal{R}_{0,\text{LVK}}$  is obtained. The steepening of the delay-time distribution rapidly decreases the local merger rate density. Figure 10 shows the results for  $dp/dt_d \propto t_d^{-1.5}$ . The agreement with the observed value is now much easier to reach, especially for the assumption  $Z_{\text{O/H},0} = 9.2$ . In some cases, the choice of  $Z_{\text{O/H},0} = 9.2$  even leads to underestimating the rates.

Realistic metallicity relations with  $Z_{\text{O/H},0} = 9.0$ ,  $a_{\text{MZR}} = 0.15$ ,  $\nabla_{\text{FMR},0} = 0.2 - 0.3$  can now reproduce the local merger rate density within a factor  $\sim 2$ . This happens because a steepening of the delay time distribution implies that more BBHs merge sooner after their formation and the contribution to the local BBH merger rate coming from objects formed at high redshift is reduced. This is important, as a substantial fraction of the local BBH merger rate is contributed by objects formed at  $z \sim 2$ , where there is the peak of the cosmic SFR of the Universe.

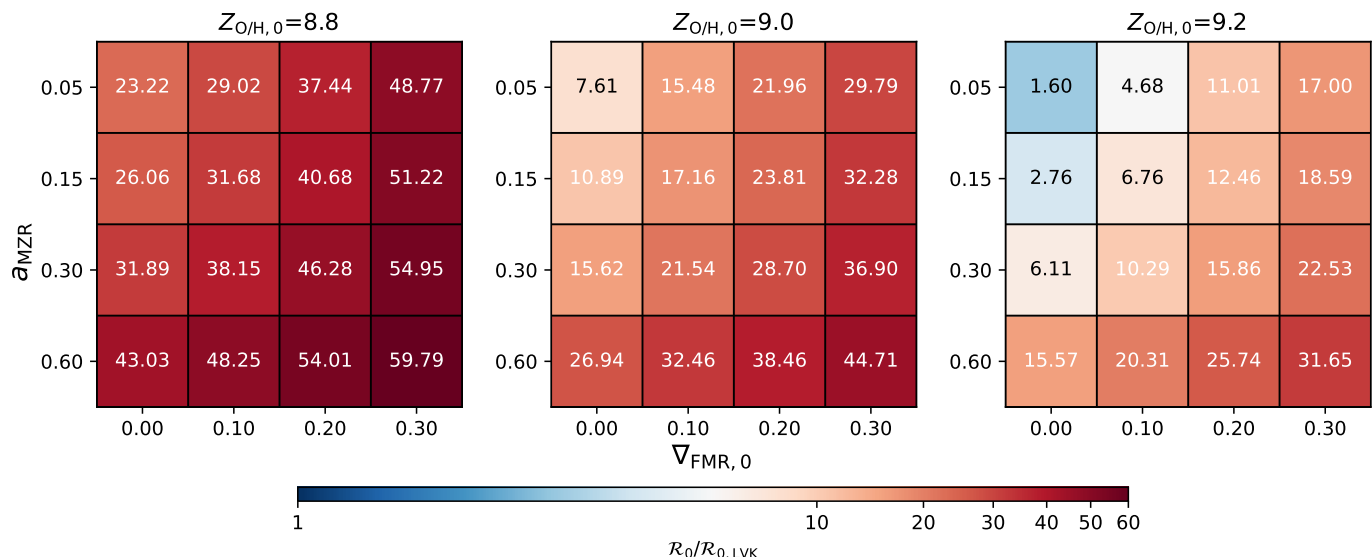


**Fig. 8.** Same as Figure 6, but for an extended range of parameters.  $R_{0,LVK}$  can be marginally matched only for unrealistic values of  $Z_{O/H,0} = 9.2$ ,  $V_{FMR,0} = 0$  and  $a_{MZR} = 0.05, 0.15$ .

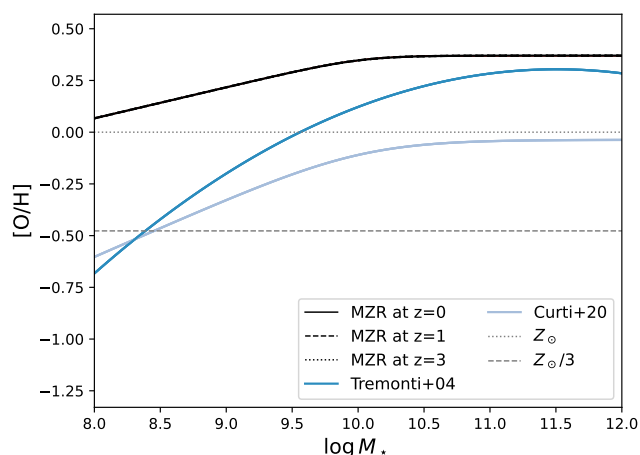


**Fig. 9.** The MZR for  $Z_{O/H,0} = 9.2$ ,  $V_{FMR,0} = 0$ , and  $a_{MZR} = 0.15$ . Blue solid, dashed and dotted lines show the MZR at  $z = 0, 1, 3$ , but they are superimposed since the MZR does not evolve with redshift for  $V_{FMR,0} = 0$ . The two blue lines are classical  $z = 0$  MZR from the literature: Tremonti et al. (2004) dark blue, Curti et al. (2020) steel blue. The gray dashed and dotted horizontal lines represent  $Z_{\odot}/3$  and  $Z_{\odot}$ . Unrealistically high values of metallicity are needed to reproduce the local BBH merger rate density, especially for low-mass galaxies.

However, we caution that the results of this section are meant just as a toy model of the behavior that binary population simulations should exhibit in order to reconcile the predicted  $R_0$  with observations, not as a solution to the problem. Indeed, the approach of separately varying the merger efficiency or delay time is intrinsically inconsistent. Since the merger efficiency is defined as the number of BBH mergers in an Hubble time,  $t_H$ , divided by the total mass of the stellar population, its value is strongly connected to the shape of the delay time distribution:

$$\eta(Z) \equiv \frac{1}{M_{\text{pop}}} \int_{t_{d,\min}}^{t_H} dt_d \frac{dN}{dt_d}(t_d|Z) \quad (6)$$

If the number of BBHs formed is fixed, a steeper delay-time distribution results in a larger merger efficiency  $\eta(Z)$ , because a larger fraction of systems have delay times  $t_d < t_H$  and therefore merge within a Hubble time. Conversely, a shallower delay-time distribution leads to a smaller value of  $\eta(Z)$  as a smaller fraction of systems satisfy  $t_d > t_H$ .

The pronounced decline in merger efficiency at high metallicities can be explained almost entirely by the corresponding change in the shape of the delay-time distribution, which becomes shallower with increasing metallicity. This behavior is clearly illustrated by Iorio et al. (2023) (see their Fig. 17), who show that the BBH formation efficiency,  $\eta_{\text{form}}$ , decreases only by a factor of  $\sim 2$  across the full metallicity range. In contrast, the merger efficiency,  $\eta$ , drops by more than three orders of magnitude at  $Z \gtrsim Z_{\odot}/3$ . This difference can be entirely attributed to the behavior of the delay-time distribution.

This interplay between merger efficiency and delay-time distribution produces a compensation effect in the computation of the local BBH merger rates: shorter delay time distributions imply higher merger efficiency, but less systems with long delay times, thereby suppressing the contribution of BBHs formed at cosmic noon ( $z \sim 2$ ) to the local merger rate. Conversely, a shallower delay-time distribution decreases the merger efficiency but enhances the contribution to the local merger rate of BBHs formed at the peak of star formation activity (see e.g. Figure 11 of Santoliquido et al. (2021)).

#### 4.3. Comparison with previous works

Several studies estimate the BBH merger rate density, locally and at high redshift (O’Shaughnessy et al. 2010; Dominik et al. 2013; Belczynski et al. 2016; Lamberts et al. 2016; Mapelli et al. 2017; O’Shaughnessy et al. 2017; Lamberts et al. 2018; Mapelli & Giacobbo 2018; Kruckow et al. 2018; Bray & Eldridge 2018; Cao et al. 2018; Elbert et al. 2018; Li et al. 2018; Boco et al. 2019; Artale et al. 2019; Neijssel et al. 2019; Tang et al. 2020; Santoliquido et al. 2020; Boco et al. 2021; Santoliquido et al. 2021; Mapelli et al. 2021; Olejak et al. 2021; Broekgaarden et al. 2021, 2022; Santoliquido et al. 2022; Ghodla et al. 2022; Briel et al. 2023; Iorio et al. 2023; Romagnolo et al.

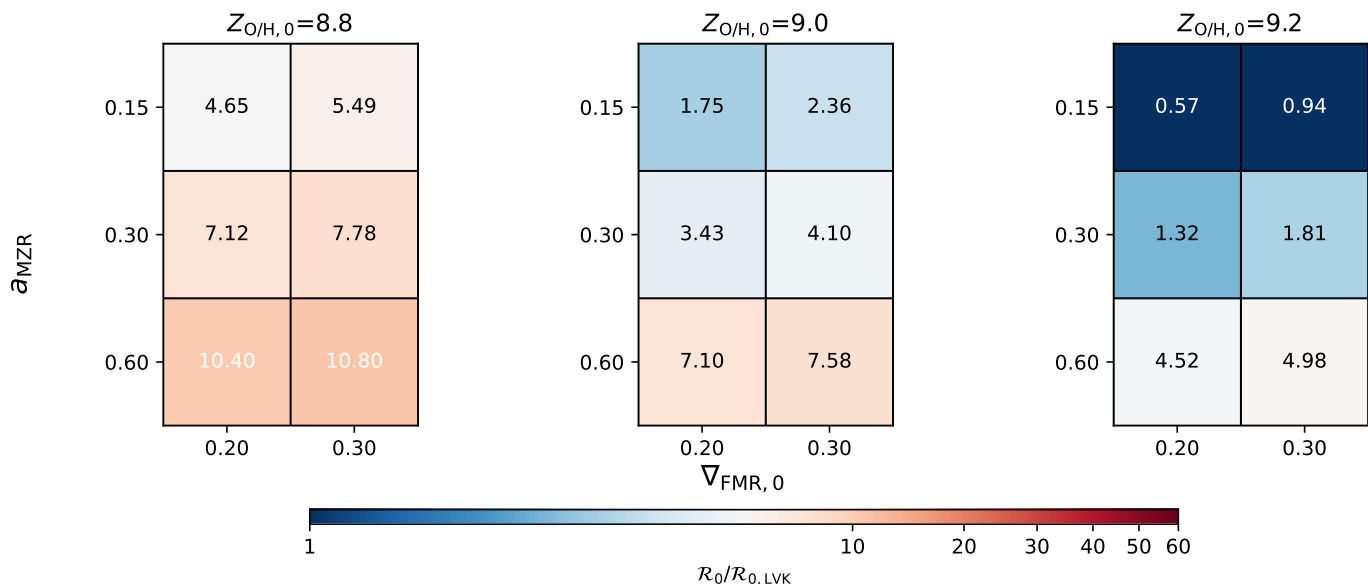


**Fig. 10.** Same as Figure 6, but for  $dp/dt_d \propto t_d^{-1.5}$ .  $\mathcal{R}_{0,LVK}$  can be matched for a large set of metallicity parameters.

2023, 2025; Sgalletta et al. 2025; Levina et al. 2026). Since the computation involves modeling of several physical processes, many assumptions, choices and parameters, performing a thorough comparison of all the results is complex. However, since some of the model variations do find a local BBH merger rate  $\lesssim 20 \text{ Gpc}^{-3} \text{ yr}^{-1}$ , it is instructive to analyze the main reasons leading to such low merger rates in some models. We use the review by Mandel & Broekgaarden (2022) as a guidance through the  $\mathcal{R}_0$  estimations of different works (see their Figure 3). The studies reported there investigate different model variations for both the stellar and binary evolution term and the metallicity-dependent SFRD, obtaining a large range of  $\mathcal{R}_0$  values. Most of the works predict  $\mathcal{R}_0 \gtrsim 100 \text{ Gpc}^{-3} \text{ yr}^{-1}$ , but some of them feature model variations extending to  $\mathcal{R}_0 \lesssim 20 \text{ Gpc}^{-3} \text{ yr}^{-1}$ . Here, we consider only those studies and analyze only the model variations leading to such low rates, trying to find common assumptions and features.

The reasons for the low merger rates are mainly two: (i) high natal kick velocities, and (ii) small amount of low-metallicity star formation rate. As for the natal kicks, only model variations using Hobbs et al. (2005) kick prescriptions, with  $\sigma = 265 \text{ km s}^{-1}$ , produce low  $\mathcal{R}_0$  values. This is valid for BSE (Mapelli et al. 2017), STARTRACK (Chruslinska et al. 2019; Belczynski et al. 2020), and SEVN (Sgalletta et al. 2025), while BPASS produce high local rates even with such strong kicks (Eldridge et al. 2019; Tang et al. 2020). While Hobbs et al. (2005) kicks are calibrated on neutron stars observations, though with the correction introduced by Disberg & Mandel (2025), constraining BH natal kicks is more challenging (Repetto et al. 2012, 2017; Atri et al. 2019). Historically, BH kicks have generally been assumed to be smaller than neutron star kicks because of fallback during the supernova explosion (Mirabel & Rodrigues 2003; Belczynski et al. 2010; Giacobbo & Mapelli 2018; Neijssel et al. 2019). Here, we show that neutron star-like kicks can help alleviate the overestimation of BBH merger rates. The next *Gaia* data release is going to provide useful constrains on the kicks: if kicks are modulated by fallback, there should be a large population of dormant BHs in large period binaries that the next *Gaia* data release should observe (Mapelli et al. 2026). A non-detection of such popula-

tion by *Gaia* would favor stronger BH natal kicks, similar to the ones inferred for Galactic neutron stars.

As for the metal-dependent SFRD, low BBH merger rates are obtained by models with no or low scatter around the metallicity relation (Dominik et al. 2013; Santoliquido et al. 2020, 2021; Mapelli et al. 2021; Iorio et al. 2023). In particular, most of these models use a cosmic averaged metallicity, i.e. an average metallicity at each redshift, with a fixed scatter, usually assumed to follow a Gaussian  $\log Z$  distribution with  $\sigma \sim 0.2$  dex, underestimating low-metallicity tails due to low-mass galaxies. This can be seen in Figure 4 of Santoliquido et al. (2022), which compares the dispersion in metallicity between models following a FMR or MZR and cosmic averaged models. Also Tang et al. (2020) shows that  $\mathcal{R}_0 \lesssim 20 \text{ Gpc}^{-3} \text{ yr}^{-1}$  can be obtained only for  $\beta \gtrsim 4$  (see their Eq. 4), corresponding to very low scatter in the cosmic averaged metallicity. Some of the models also assume fixed (Kruckow et al. 2018), sometimes very high (O’Shaughnessy et al. 2010; Bray & Eldridge 2018) metallicities, with no redshift evolution.

A useful overview of how metallicity impacts the local BBH merger rate density can be found in Broekgaarden et al. (2022). Most of the models reported there tend to produce  $\mathcal{R}_0 > 20 \text{ Gpc}^{-3} \text{ yr}^{-1}$ . The only models matching  $\mathcal{R}_0 \sim 20 \text{ Gpc}^{-3} \text{ yr}^{-1}$  are those with very high average metallicities. This is clearly shown in their Figs. A2 and in Fig. B1 (Broekgaarden et al. 2021), where their model with the lowest merger rates is shown to have average metallicity  $Z \sim Z_{\odot}/2$  up to  $z \sim 3$ . Finally, in most of the works mentioned above, oxygen abundances were used to derive metallicity, further underestimating the merger rates.

The only works with low BBH merger rate density not directly linked to high kicks or to the metallicity modelization involve either revised common-envelope development criteria (Olejak et al. 2021) or a different treatment of rejuvenation during mass transfer (Ghodla et al. 2022; Briel et al. 2023).

Despite the different modelization present in the works, both on the galaxy evolution side and on the binary evolution one, we conclude that these results are in line with the main message of this paper: predicted local BBH merger rates can be reconciled with observations only via a reduction of the BBH merger efficiency, e.g. via the increase of the strength of natal kicks, or a

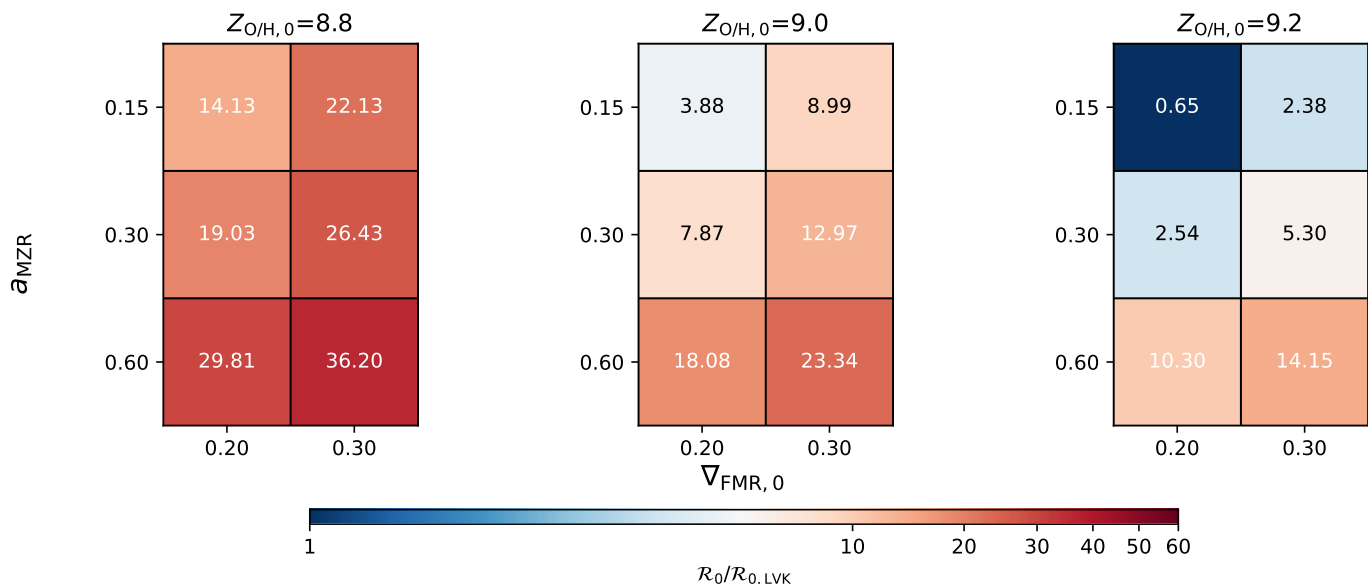


Fig. 11. Same as Figure 6, but using oxygen abundances.

different treatment of mass transfer and common-envelope evolution in binary population synthesis codes.

#### 4.4. Impact of iron abundance

Finally, we investigate the impact on  $\mathcal{R}_0$  of adopting iron abundance rather than oxygen. In Figure 11, we present results obtained using oxygen abundances, without the correction for [O/Fe]. Even in this case, most models still overestimate  $\mathcal{R}_0$ ; however, for some configurations with  $Z_{O/H,0} = 9.2$ , the observed local merger rate density, can be reproduced within a factor of  $\sim 2$ . We conclude that the choice of iron rather than oxygen abundance has a substantial impact, significantly exacerbating the tension between models and observations. In particular, variations yielding the highest metallicities are more affected by the use of iron abundances. This is because iron abundance introduces the necessary scatter to allow a non-negligible fraction of star formation to occur at low metallicities ( $Z < Z_{\odot}/3$ ), thereby increasing the predicted BBH merger rate density.

## 5. Summary

We estimated the BBH merger rate density from the isolated binary-evolution channel using empirical relations to compute the metallicity-dependent SFRD and combining it with the outcomes of the binary population synthesis code *SEVN*. For the first time in an empirical approach, we have used iron abundances rather than oxygen abundances to perform the computation. Our main findings are the following.

- The predicted local BBH merger rate density is higher than the observed  $\mathcal{R}_{0,LVK} \sim 14 - 26 \text{ Gpc}^{-3} \text{ yr}^{-1}$  for any reasonable variation of the fundamental metallicity relation by a factor  $> 10$ . This is true even if the metallicity-dependent SFRD is built with the aim of minimizing local BBH merger rates.
- Reconciling the predicted and observed  $\mathcal{R}_0$  value would require extremely high metallicities,  $\sim Z_{\odot}$ , even for low-mass galaxies  $\sim 10^8 M_{\odot}$  at high redshift.
- Changing the common-envelope efficiency parameter  $\alpha_{CE}$  alleviates the problem, but even extreme values as  $\alpha_{CE} = 10$

yield  $\mathcal{R}_0/\mathcal{R}_{0,LVK} \gtrsim 3$  only for the most optimistic metallicity variations.

- A reduction of the merger efficiency by a factor of  $\sim 10$  or a steepening of the delay-time distribution to  $dp/dt_d \propto t_d^{-1.5}$  is needed in order to reconcile the predicted and observed local merger rate density.
- Using iron abundance instead of oxygen abundance [Ch25](#) has a large impact on the estimated merger rate density and worsens the tension with data by a factor  $\sim 2 - 10$  depending on the metallicity variation.

Overall, our results show that variations of the metallicity-dependent SFRD within the limits allowed by observations are not enough to reconcile the predicted and observed local BBH merger rate density. We advocate that modifications to the treatment of stellar and binary evolution are necessary to obtain successful predictions. Some possibilities include higher natal kicks, a revised treatment of mass transfer and common-envelope evolution, and/or a revised treatment of massive stars' winds. In future works, we will explore some of these options and their effects on the merger rate and on the properties of binary compact objects.

*Acknowledgements.* LB thanks Stefano Torniamenti for useful discussions. LB acknowledges support by the Deutsche Forschungsgemeinschaft (DFG, German Research Foundation) in the form of a Walter Benjamin position – Projekt-nummer 555003977. LB and MM acknowledge financial support from the German Excellence Strategy via the Heidelberg Cluster of Excellence (EXC 2181 - 390900948) STRUCTURES. MM acknowledges financial support from the European Research Council for the ERC Consolidator grant DEMOBLOCK, under contract no. 770017. MB acknowledges that this article was produced while attending the PhD program in PhD in Space Science and Technology at the University of Trento, Cycle XXXIX, with the support of a scholarship financed by the Ministerial Decree no. 118 of 2nd March 2023, based on the NRRP - funded by the European Union - NextGenerationEU - Mission 4 "Education and Research". Component 1 "Enhancement of the offer of educational services: from nurseries to universities" - Investment 4.1 "Extension of the number of research doctorates and innovative doctorates for public administration and cultural heritage" - CUP E66E23000110001 and support by the Italian grant Project SPACE-IT-UP by the Italian Space Agency and Ministry of University and Research, Contract Number 2024-5-E.0. This research made use of NUMPY ([Harris et al. 2020](#)), SCIPY ([Virtanen et al. 2020](#)), and MATPLOTLIB ([Hunter 2007](#)). We used SEVN (<https://gitlab.com/sevncodes/sevn>) to generate our BBHs catalogs ([Spera et al. 2019](#); [Mapelli et al. 2020](#); [Iorio et al. 2023](#)).

## References

- Álvarez, C. A., Cueli, M. M., Bressan, A., et al. 2025, *A&A*, 703, A26
- Andrews, B. H. & Martini, P. 2013, *ApJ*, 765, 140
- Antoniadis, K., Zapartas, E., Bonanos, A. Z., et al. 2025, *A&A*, 702, A178
- Artale, M. C., Mapelli, M., Giacobbo, N., et al. 2019, *MNRAS*, 487, 1675
- Atri, P., Miller-Jones, J. C. A., Bahramian, A., et al. 2019, *MNRAS*, 489, 3116
- Belczynski, K., Dominik, M., Bulik, T., et al. 2010, *ApJ*, 715, L138
- Belczynski, K., Kléncki, J., Fields, C. E., et al. 2020, *A&A*, 636, A104
- Belczynski, K., Repetto, S., Holz, D. E., et al. 2016, *ApJ*, 819, 108
- Bellstedt, S., Robotham, A. S. G., Driver, S. P., et al. 2024, *MNRAS*, 528, 5452
- Bestenlehner, J. M. 2020, *MNRAS*, 493, 3938
- Bestenlehner, J. M., Gräfenor, G., Vink, J. S., et al. 2014, *A&A*, 570, A38
- Béthermin, M., Daddi, E., Magdis, G., et al. 2012, *ApJ*, 757, L23
- Bisigello, L., Caputi, K. I., Grogin, N., & Koekemoer, A. 2018, *A&A*, 609, A82
- Boco, L., Lapi, A., Chruslinska, M., et al. 2021, *ApJ*, 907, 110
- Boco, L., Lapi, A., Goswami, S., et al. 2019, *ApJ*, 881, 157
- Boco, L., Mapelli, M., Sander, A. A. C., et al. 2025, *A&A*, 703, A243
- Bosi, M., Lapi, A., Boco, L., et al. 2025, *ApJ*, 984, 117
- Brands, S. A., Backs, F., de Koter, A., et al. 2025, *A&A*, 697, A54
- Brands, S. A., de Koter, A., Bestenlehner, J. M., et al. 2022, *A&A*, 663, A36
- Bray, J. C. & Eldridge, J. J. 2018, *MNRAS*, 480, 5657
- Briel, M. M., Stevance, H. F., & Eldridge, J. J. 2023, *MNRAS*, 520, 5724
- Broekgaarden, F. S., Berger, E., Neijssel, C. J., et al. 2021, *MNRAS*, 508, 5028
- Broekgaarden, F. S., Berger, E., Stevenson, S., et al. 2022, *MNRAS*, 516, 5737
- Cao, L., Lu, Y., & Zhao, Y. 2018, *MNRAS*, 474, 4997
- Caputi, K. I., Deshmukh, S., Ashby, M. L. N., et al. 2017, *ApJ*, 849, 45
- Chiappini, C., Matteucci, F., & Gratton, R. 1997, *ApJ*, 477, 765
- Chruślińska, M., Curti, M., Pakmor, R., et al. 2025, arXiv e-prints, arXiv:2511.15782
- Chruslinska, M. & Nelemans, G. 2019, *MNRAS*, 488, 5300
- Chruslinska, M., Nelemans, G., & Belczynski, K. 2019, *MNRAS*, 482, 5012
- Chruślińska, M., Nelemans, G., Boco, L., & Lapi, A. 2021, *MNRAS*, 508, 4994
- Chruślińska, M., Pakmor, R., Matthee, J., & Matsuno, T. 2024, *A&A*, 686, A186
- Courteau, S., Cappellari, M., de Jong, R. S., et al. 2014, *Reviews of Modern Physics*, 86, 47
- Cresci, G., Mannucci, F., & Curti, M. 2019, *A&A*, 627, A42
- Cullen, F., Shapley, A. E., McLure, R. J., et al. 2021, *MNRAS*, 505, 903
- Curti, M., D'Eugenio, F., Carniani, S., et al. 2023, *MNRAS*, 518, 425
- Curti, M., Mannucci, F., Cresci, G., & Maiolino, R. 2020, *MNRAS*, 491, 944
- Daddi, E., Alexander, D. M., Dickinson, M., et al. 2007, *ApJ*, 670, 173
- Davidzon, I., Ilbert, O., Laigle, C., et al. 2017, *A&A*, 605, A70
- Disberg, P. & Mandel, I. 2025, *ApJ*, 989, L8
- Dominik, M., Belczynski, K., Fryer, C., et al. 2013, *ApJ*, 779, 72
- Dunlop, J. S., McLure, R. J., Biggs, A. D., et al. 2017, *MNRAS*, 466, 861
- Elbert, O. D., Bullock, J. S., & Kaplinghat, M. 2018, *MNRAS*, 473, 1186
- Eldridge, J. J., Stanway, E. R., & Tang, P. N. 2019, *MNRAS*, 482, 870
- Fuller, J. & Tsuna, D. 2024, *The Open Journal of Astrophysics*, 7, 47
- Gallazzi, A., Charlot, S., Brinchmann, J., & White, S. D. M. 2006, *MNRAS*, 370, 1106
- Ghodla, S., van Zeist, W. G. J., Eldridge, J. J., Stevance, H. F., & Stanway, E. R. 2022, *MNRAS*, 511, 1201
- Giacobbo, N. & Mapelli, M. 2018, *MNRAS*, 480, 2011
- Gornaz-Matamala, A. C., Romagnolo, A., & Belczynski, K. 2025, *A&A*, 696, A72
- Grevesse, N. & Sauval, A. J. 1998, *Space Sci. Rev.*, 85, 161
- Harris, C. R., Millman, K. J., van der Walt, S. J., et al. 2020, *Nature*, 585, 357
- Hobbs, G., Lorimer, D. R., Lyne, A. G., & Kramer, M. 2005, *MNRAS*, 360, 974
- Hunt, L., Dayal, P., Magrini, L., & Ferrara, A. 2016, *MNRAS*, 463, 2002
- Hunter, J. D. 2007, *Computing in Science and Engineering*, 9, 90
- Ilbert, O., Arnouts, S., Le Floch, E., et al. 2015, *A&A*, 579, A2
- Ilbert, O., McCracken, H. J., Le Fèvre, O., et al. 2013, *A&A*, 556, A55
- Iorio, G., Mapelli, M., Costa, G., et al. 2023, *MNRAS*, 524, 426
- Johansson, J., Thomas, D., & Maraston, C. 2012, *MNRAS*, 421, 1908
- Kee, N. D., Sundqvist, J. O., Decin, L., de Koter, A., & Sana, H. 2021, *A&A*, 646, A180
- Kewley, L. J. & Dopita, M. A. 2002, *ApJS*, 142, 35
- Kobulnicky, H. A. & Kewley, L. J. 2004, *ApJ*, 617, 240
- Kruckow, M. U., Tauris, T. M., Langer, N., Kramer, M., & Izard, R. G. 2018, *MNRAS*, 481, 1908
- Lamberts, A., Garrison-Kimmel, S., Clausen, D. R., & Hopkins, P. F. 2016, *MNRAS*, 463, L31
- Lamberts, A., Garrison-Kimmel, S., Hopkins, P. F., et al. 2018, *MNRAS*, 480, 2704
- Lapi, A., Pantoni, L., Boco, L., & Danese, L. 2020, *ApJ*, 897, 81
- Lara-López, M. A., Cepa, J., Bongiovanni, A., et al. 2010, *A&A*, 521, L53
- Levina, S., Broekgaarden, F., van Son, L., et al. 2026, arXiv e-prints, arXiv:2601.20202
- Li, S.-S., Mao, S., Zhao, Y., & Lu, Y. 2018, *MNRAS*, 476, 2220
- Maiolino, R. & Mannucci, F. 2019, *A&A Rev.*, 27, 3
- Maiolino, R., Nagao, T., Grazian, A., et al. 2008, *A&A*, 488, 463
- Mancuso, C., Lapi, A., Shi, J., et al. 2016, *ApJ*, 833, 152
- Mandel, I. & Broekgaarden, F. S. 2022, *Living Reviews in Relativity*, 25, 1
- Mannucci, F., Cresci, G., Maiolino, R., Marconi, A., & Gnerucci, A. 2010, *MNRAS*, 408, 2115
- Mannucci, F., Cresci, G., Maiolino, R., et al. 2009, *MNRAS*, 398, 1915
- Mannucci, F., Salvaterra, R., & Campisi, M. A. 2011, *MNRAS*, 414, 1263
- Mapelli, M. & Giacobbo, N. 2018, *MNRAS*, 479, 4391
- Mapelli, M., Giacobbo, N., Ripamonti, E., & Spera, M. 2017, *MNRAS*, 472, 2422

- Mapelli, M., Santoliquido, F., Bouffanais, Y., et al. 2021, *Symmetry*, 13, 1678
- Mapelli, M., Sgalletta, C., Müller-Horn, J., et al. 2026, arXiv e-prints, arXiv:2604.12839
- Mapelli, M., Spera, M., Montanari, E., et al. 2020, *ApJ*, 888, 76
- Mirabel, I. F. & Rodrigues, I. 2003, *Science*, 300, 1119
- Muzzin, A., Marchesini, D., Stefanon, M., et al. 2013, *ApJ*, 777, 18
- Nakajima, K., Ouchi, M., Isobe, Y., et al. 2023, *ApJS*, 269, 33
- Neijssel, C. J., Vigna-Gómez, A., Stevenson, S., et al. 2019, *MNRAS*, 490, 3740
- Olejak, A., Belczynski, K., & Ivanova, N. 2021, *A&A*, 651, A100
- O’Shaughnessy, R., Bellovary, J. M., Brooks, A., et al. 2017, *MNRAS*, 464, 2831
- O’Shaughnessy, R., Kalogera, V., & Belczynski, K. 2010, *ApJ*, 716, 615
- Pantoni, L., Lapi, A., Massardi, M., Goswami, S., & Danese, L. 2019, *ApJ*, 880, 129
- Pettini, M. & Pagel, B. E. J. 2004, *MNRAS*, 348, L59
- Pezzulli, G. & Fraternali, F. 2016, *MNRAS*, 455, 2308
- Popesso, P., Concas, A., Cresci, G., et al. 2023, *MNRAS*, 519, 1526
- Repetto, S., Davies, M. B., & Sigurdsson, S. 2012, *MNRAS*, 425, 2799
- Repetto, S., Igoshev, A. P., & Nelemans, G. 2017, *MNRAS*, 467, 298
- Rinaldi, P., Caputi, K. I., van Mierlo, S. E., et al. 2022, *ApJ*, 930, 128
- Rinaldi, P., Navarro-Carrera, R., Caputi, K. I., et al. 2025, *ApJ*, 981, 161
- Rodighiero, G., Brusa, M., Daddi, E., et al. 2015, *ApJ*, 800, L10
- Rodighiero, G., Daddi, E., Baronchelli, I., et al. 2011, *ApJ*, 739, L40
- Romagnolo, A., Belczynski, K., Klencki, J., et al. 2023, *MNRAS*, 525, 706
- Romagnolo, A., Broekgaarden, F. S., Antoniadis, K., & Gormaz-Matamala, A. C. 2026, arXiv e-prints, arXiv:2601.02263
- Romagnolo, A., Gormaz-Matamala, A. C., & Belczynski, K. 2024, *ApJ*, 964, L23
- Romagnolo, A., Klencki, J., Vigna-Gómez, A., & Belczynski, K. 2025, *A&A*, 693, A137
- Sabhahit, G. N., Vink, J. S., Higgins, E. R., & Sander, A. A. C. 2022, *MNRAS*, 514, 3736
- Sabhahit, G. N., Vink, J. S., Sander, A. A. C., & Higgins, E. R. 2023, *MNRAS*, 524, 1529
- Salim, S., Lee, J. C., Ly, C., et al. 2014, *ApJ*, 797, 126
- Sana, H., de Mink, S. E., de Koter, A., et al. 2012, *Science*, 337, 444
- Sanders, R. L., Shapley, A. E., Jones, T., et al. 2021, *ApJ*, 914, 19
- Sanders, R. L., Shapley, A. E., Kriek, M., et al. 2018, *ApJ*, 858, 99
- Santoliquido, F., Mapelli, M., Artale, M. C., & Boco, L. 2022, *MNRAS*, 516, 3297
- Santoliquido, F., Mapelli, M., Bouffanais, Y., et al. 2020, *ApJ*, 898, 152
- Santoliquido, F., Mapelli, M., Giacobbo, N., Bouffanais, Y., & Artale, M. C. 2021, *MNRAS*, 502, 4877
- Sargent, M. T., Béthermin, M., Daddi, E., & Elbaz, D. 2012, *ApJ*, 747, L31
- Schreiber, C., Pannella, M., Elbaz, D., et al. 2015, *A&A*, 575, A74
- Sgalletta, C., Mapelli, M., Boco, L., et al. 2025, *A&A*, 698, A144
- Shepherd, K. G., Costa, G., Ugolini, C., et al. 2025, *A&A*, 701, A126
- Shuntov, M., Akins, H. B., Paquereau, L., et al. 2025, *A&A*, 704, A339
- Simonato, F., Torniamenti, S., Mapelli, M., et al. 2025, *A&A*, 703, A215
- Speagle, J. S., Steinhardt, C. L., Capak, P. L., & Silverman, J. D. 2014, *ApJS*, 214, 15
- Spera, M., Mapelli, M., Giacobbo, N., et al. 2019, *MNRAS*, 485, 889
- Steidel, C. C., Rudie, G. C., Strom, A. L., et al. 2014, *ApJ*, 795, 165
- Steidel, C. C., Strom, A. L., Pettini, M., et al. 2016, *ApJ*, 826, 159
- Strom, A. L., Rudie, G. C., Steidel, C. C., & Trainor, R. F. 2022, *ApJ*, 925, 116
- Tang, P. N., Eldridge, J. J., Stanway, E. R., & Bray, J. C. 2020, *MNRAS*, 493, L6
- The LIGO Scientific Collaboration, the Virgo Collaboration, the KAGRA Collaboration, et al. 2025, arXiv e-prints, arXiv:2508.18083
- Thomas, D., Maraston, C., Bender, R., & Mendes de Oliveira, C. 2005, *ApJ*, 621, 673
- Thomas, D., Maraston, C., Schawinski, K., Sarzi, M., & Silk, J. 2010, *MNRAS*, 404, 1775
- Tomczak, A. R., Quadri, R. F., Tran, K.-V. H., et al. 2014, *ApJ*, 783, 85
- Topping, M. W., Shapley, A. E., Reddy, N. A., et al. 2020, *MNRAS*, 499, 1652
- Torniamenti, S., Mapelli, M., Boco, L., et al. 2026, *A&A*, 707, A38
- Torrey, P., Vogelsberger, M., Hernquist, L., et al. 2018, *MNRAS*, 477, L16
- Tremonti, C. A., Heckman, T. M., Kauffmann, G., et al. 2004, *ApJ*, 613, 898
- van Son, L. A. C., de Mink, S. E., Chruślińska, M., et al. 2023, *ApJ*, 948, 105
- van Son, L. A. C., Roy, S. K., Mandel, I., et al. 2025, *ApJ*, 979, 209
- Vink, J. S., Muijres, L. E., Anthonisse, B., et al. 2011, *A&A*, 531, A132
- Virtanen, P., Gommers, R., Oliphant, T. E., et al. 2020, *Nature Methods*, 17, 261
- Weaver, J. R., Davidzon, I., Toft, S., et al. 2023, *A&A*, 677, A184
- Whitaker, K. E., Franx, M., Leja, J., et al. 2014, *ApJ*, 795, 104
- Zahid, H. J., Dima, G. I., Kudritzki, R.-P., et al. 2014, *ApJ*, 791, 130

## Appendix A: Choice of the metallicity parameters

In Section 2.3 we introduced the FMR functional form and we explained how we can compute its parameters from the local MZR and main sequence. We also introduced the three free metallicity parameters used to compute the others:  $\nabla_{\text{FMR},0}$ ,  $a_{\text{MZR}}$ , and  $Z_{\text{O/H},0}$  and we provided the values used for these parameters in Table 1. In this Appendix, we motivate this choice, showing that those values encompass most of the values found in literature.

The slope of the local MZR,  $a_{\text{MZR}}$  has been studied by several authors (Kewley & Dopita 2002; Tremonti et al. 2004; Maiolino et al. 2008; Mannucci et al. 2009; Andrews & Martini 2013; Zahid et al. 2014; Curti et al. 2020; Sanders et al. 2021). Most recent studies (Curti et al. 2020; Sanders et al. 2021) favor shallower values  $\sim 0.3$  than those found in previous ones  $\sim 0.6$  (Andrews & Martini 2013; Zahid et al. 2014). These values are found by fitting the metallicity as a function of the stellar mass irrespectively of the galaxy SFR.  $a_{\text{MZR}}$  in the range 0.3 – 0.6 is adopted even in Ch21 for their explorations. However, we notice that most of the FMR reported in literature (e.g., Andrews & Martini 2013; Hunt et al. 2016; Curti et al. 2020) imply even shallower values of  $a_{\text{MZR}}$  when coupled with the main sequence Popesso et al. (2023). This is because Popesso et al. (2023) main sequence features a steep faint-end slope  $a_{\text{MS}} \sim 1$ . This means that to an increase in  $M_{\star}$  corresponds a relatively large SFR increase, thus weakening the metallicity dependence on  $M_{\star}$ . For example, the FMR of Andrews & Martini (2013) features  $\gamma = 0.43$ ,  $\nabla_{\text{FMR},0} \sim 0.27$  and that of Curti et al. (2020)  $\gamma = 0.31$ ,  $\nabla_{\text{FMR},0} \sim 0.17$ , corresponding to  $a_{\text{MZR}} \sim 0.15$  in the case  $a_{\text{MS}} = 1^3$ . To bracket all the possible range of uncertainty, in this work, we show results for  $a_{\text{MZR}} = 0.15, 0.3, 0.6$ .

$\nabla_{\text{FMR},0}$  represents the strength of the anti-correlation between metallicity and SFR. Several works estimate its value but the results are dependent on metallicity calibration and/or redshift (Salim et al. 2014; Sanders et al. 2018; Torrey et al. 2018; Sanders et al. 2021). Most of these works report values ranging between 0.2 – 0.3, with some exception for specific mass or redshift bins arriving at  $\nabla_{\text{FMR},0} \gtrsim 0.1$  (see Ch21 for a thorough discussion). However, Ch21 find that values  $\nabla_{\text{FMR},0} \lesssim 0.17$  underpredict both the redshift evolution of the MZR at  $z \lesssim 1.5$  and the scatter of the MZR. For these reasons, here we show results for  $\nabla_{\text{FMR},0} = 0.2, 0.3$ .

We also vary the overall normalization of the FMR  $Z_{\text{O/H},0}$ . Direct method measurements of gas phase metallicity (Pettini & Pagel 2004; Curti et al. 2020; Sanders et al. 2021) derive  $Z_{\text{O/H},0} \sim 8.8$ , which is lower with respect to the values found using theoretical calibrations  $Z_{\text{O/H},0} \sim 9.1$  (Kewley & Dopita 2002; Tremonti et al. 2004; Kobulnicky & Kewley 2004; Mannucci et al. 2010). This reflects a longstanding issue where direct methods tend to underestimate oxygen abundance, while theoretical models tend to overestimate it (Maiolino & Mannucci 2019). Chruślińska et al. (2024, 2025) show that, in order to reconcile the average [O/Fe] of young star-forming galaxies and old Milky Way stars, a shift of 0.2 above the direct method estimates might be necessary. In this work we show results for  $Z_{\text{O/H},0} = 8.8, 9.0, 9.2$ , so to encompass all the possible values of  $Z_{\text{O/H},0}$ .

<sup>3</sup> Note that these two works present also determinations of the MZR by stacking together galaxies with the same stellar mass and different SFR. They find higher  $a_{\text{MZR}}$  values ( $\sim 0.3$  for Andrews & Martini (2013), and  $\sim 0.6$  for Curti et al. (2020)). The difference with respect to  $a_{\text{MZR}} \sim 0.15$  is due to the galaxy sample chosen, which feature a much shallower dependence of SFR on  $M_{\star}$  than the Popesso et al. (2023) main sequence.